

Unveiling the Phase Diagram and Nonlinear Optical Responses of a Twisted Kitaev Chain

Ya-Min Quan^{1†}, Shi-Qing Jia², Xiang-Long Yu³, Hai-Qing Lin⁴ and Liang-Jian Zou^{1*}

¹ *Key Laboratory of Materials Physics,*

Institute of Solid State Physics, HFIPS,

Chinese Academy of Sciences, Hefei 230031, China

² *Department of Applied Physics, North China University*

of Science and Technology, Tangshan 063210, China

³ *School of Science, Sun Yat-sen University, Shenzhen 518107, China*

⁴ *Institute for Advanced Study in Physics and School of Physics,*

Zhejiang University, Hangzhou, 310058, China

(Dated: today)

[1] Electronic mail:zou@theory.issp.ac.cn
[2] Electronic mail:ymquan@theory.issp.ac.cn

Abstract

Detecting Kitaev interactions in real materials remains challenge, as conventional experimental techniques often have difficulty distinguishing fractionalized excitations from other normal contributions. Terahertz two-dimensional coherent spectroscopy (2DCS) offers a novel approach for probing many-body phenomena, such as exotic excitations in quantum magnets. Motivated by recent experiments on CoNb_2O_6 and the development of the terahertz spectroscopy in Kitaev quantum spin liquid, we proposed a twisted Kitaev model for CoNb_2O_6 and determined the precise twist angle according to experimental specific-heat phase diagram. With this calibrated model, we found that non-rephasing diagonal and rephasing anti-diagonal signals appear in the 2DCS nonlinear response. The x and y components of the spin superexchange interactions split the rephasing signals into a grid of discrete peaks. We further demonstrate that the diagonal and the discrete rephasing signals primarily originate from two-spinon and four-spinon excitation processes based on numerical projection method. These findings indicate that even weak Kitaev interactions in quantum materials can be effectively detected via two-dimensional coherent spectroscopy .

Keywords: twisted Kitaev model, two-dimensional coherent spectroscopy, Fractional spinon excitation

PACS numbers: 75.10.Kt, 71.30.+h, 75.10.Jm

I. INTRODUCTION

Quantum spin liquid (QSL) is a spin disordered phase of quantum matter, in which the wave function of spins is strongly entangled order and the low-energy excitations are dominated by fractionalized particles [1–3]. Kitaev model provides a precious opportunity to study QSL since it is exactly solvable and the ground state shows exotic QSL phase [4]. In recent years, experimental research on the QSL focused on 4d and 5d transition-metal oxides[5], primarily through investigating the dynamics of low-energy excitations [5–10] and thermal transport properties [11–14] in candidate QSL materials. The broad continuum spectrum observed in the dynamical probe is proposed as the signature of fractional excitations in the Kitaev QSL. But the ambiguity of other origin for continuum spectrum can not be excluded absolutely[5]. On the other hand, in the real candidate materials, the Heisenberg interaction and other non-diagonal interaction may coexist with the Kitaev interactions, leading to magnetic orders at low temperature in some candidate Kitaev materials [1, 5, 7, 15]. Besides, it is difficult to detect the effects of the Kitaev interaction in these materials by the conventional experimental methods, since there is no apparent character of fractional excitation in the spectra signature. Therefore, how to detect the Kitaev interaction in the candidate Kitaev materials remains a great challenge.

Two-dimensional coherent spectroscopy (2DCS) has been widely used to study electronic excitation and dynamics[16–18]. In 2DCS, the system is excited by three laser pulses and the subsequently coherent light emission is measured [19–21]. These signals are displayed as a function of the frequencies that obtained by performing a Fourier transformation of the time intervals. The diagonal/off-diagonal signals in the 2DCS reveal the coupling of the optical excitation and emission frequencies[19]. Since 2DCS could reflect the nonlinear responses due to multi-time correlations, it has been widely used to probe the nonlinear optical properties of molecular and semiconductor systems[22, 23]. Recently, this technology is applied to study strongly correlated many-body systems. Since the energy of THz photon falls in a proper energy range of many-body quasi-particle excitations, and the domain of the response in 2DCS is mainly determined by the character of quasi-particle excitation, it has been suggested to detect the crisp signatures of spinon and fractional excitations [20, 21, 24–26]. The itinerant Majorana fermions and flux excitations contribute to the sharp diagonal and anti-diagonal signals in 2DCS[21, 26].

On the other hand, the quasi-one-dimensional columbite CoNb_2O_6 has attracted considerable attention in recent years [27–34]. In this material, the Co^{2+} ions form a zigzag chain along the

c axis. The intrachain interaction of Co^{2+} is ferromagnetic along the easy axis, while the inter-chain coupling is very weak, leading to a complex magnetic phase diagram[35]. Experimentally, by applying a magnetic field along the *b* axis, a quantum critical point (QCP)is observed, marking a transition from a spin-ordered phase to a paramagnetic state at a critical field $B_c \approx 5.3T$ [27, 35–37]. Near the quantum critical point, the spectrum of bound states exhibits a structure corresponding to the E_8 root in the presence of a perturbing longitudinal field[36]. So it was proposed as an ideal model system of the transverse-field Ising chain [32, 34]. Meanwhile, some obvious notable deviations from the transverse-field Ising model(TFIM) behaviors displays away from the critical point[31, 38]. To account for these discrepancies, the magnon excitation spectrum observed via inelastic neutron scattering is typically described using an XXZ model incorporating NN and next-nearest-neighbor (NNN) interactions within a single cobalt spin chain [27, 39, 40]. Recently, a staggered off-diagonal exchange term has been proposed to explain the soliton spectrum[38–40]. In the quantum paramagnetic phase, the off-diagonal exchange interactions has also been used to explain the magnon decay and spectrum renormalization [40]. Additionally, Morris et al. proposed a twisted Kitaev model(TKM) with bond dependent Ising interactions for CoNb_2O_6 to interpret the deviations of absorption THz spectroscopy data from ideal TFIM[31]. This simplified model includes only the nearest-neighbor (NN) Ising-type coupling, neglecting spin exchange along the *x* and *y* directions. However, more comprehensive spin model that incorporates additional interactions is needed to reproduce the curvature of the magnon dispersion of CoNb_2O_6 [41]. All the results demonstrate that the off-diagonal interactions primarily originate from the structural twist angle and significantly influence spinon (kinks, or domain wall) domain wall dynamics. Therefore, incorporating this twist angle into the NN XXZ model enables describing the spinons dynamics in CoNb_2O_6 . Moreover, the ground state of CoNb_2O_6 is ferromagnet and it is difficult to obtain clear evidence of bond-dependent interactions from thermal transport measurements[34] or neutron scattering experiment[28]. This raises the questions of whether significant Kitaev interactions are present or not in this material, and how such bond-dependent interactions affect quasiparticle excitations. 2DCS is ideal for the study of excitations in quantum materials and it will play a key role in addressing this problem.

In this work, we explore 2DCS signatures of a TKM developed for describing the quantum material CoNb_2O_6 . We first construct a modified TKM model by introducing a twist angle into an anisotropic nearest-neighbor(NN) Heisenberg framework to characterize the magnetic interactions in CoNb_2O_6 . The twist angle is determined by comparing theoretical predictions with experimen-

tal specific heat measurements. To identify the signals induced by the Kitaev interaction, we numerically investigate the 2DCS of the modified TKM using the exact diagonalization method. We analyze the diagonal and anti-diagonal spectral features in 2DCS that arise from finite twist angles and the effect of NN XY exchange terms on these spectra, which leads to the discreteness of the rephasing spectrum (spin echo signals). Furthermore, the contributions of various multi-spinon excitations to the spectral signals are identified via projection methods. It is indicated that the two-spinon excitation is the most important process to the 2DCS. Our findings demonstrate that 2DCS serves as an effective tool for probing Kitaev interactions in quantum materials. The rest of this paper is organized as follows. In Sec. II we introduce a realistic TKM for CoNb_2O_6 and the 2DCS formalism, as well as the numerical methods used to compute the 2DCS based on Lanczos algorithm. In Sec. III we present the numerical results and discuss the Kitaev interaction features in 2DCS, the conclusion is drawn in Sec. IV.

II. MODEL HAMILTONIAN AND NUMERICAL METHOD

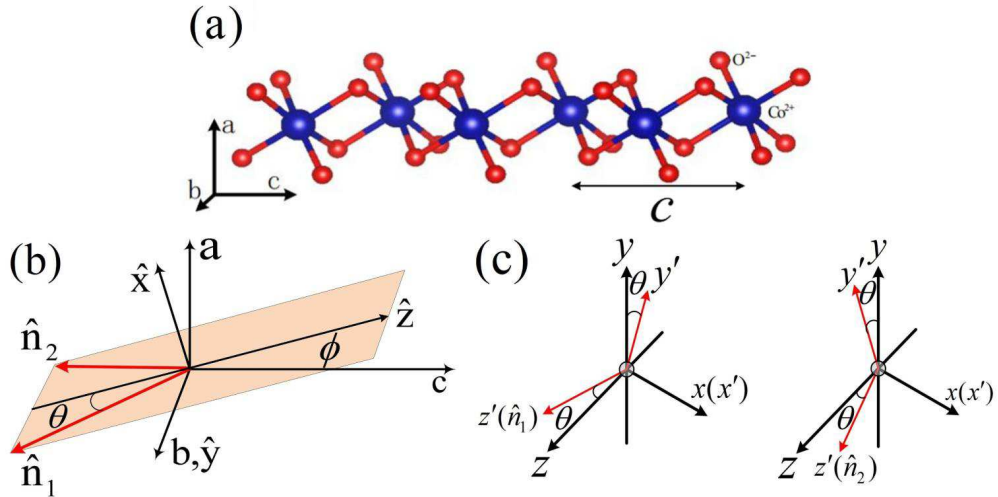


FIG. 1: (Color online) (a) The twisted Kitaev chain of Co^{2+} ions and distorted O^{2-} octahedra[31]. The crystallographic a , b , and c directions are indicated. (b) \hat{n}_1 and \hat{n}_2 are the two alternating Ising directions. The \hat{y} spin direction is identified with the b axis. θ is the twist angle that \hat{n}_1 and \hat{n}_2 made with the \hat{z} axis. (c) The laboratory reference frame $[x, y, z]$ and the local reference frame $[x', y', z']$ with z axis along the spin orientation.

CoNb_2O_6 crystallizes in an orthorhombic structure with space group $Pbcn$. Magnetic Co^{2+}

ions form one-dimensional (1D) chains in the ac plane, extending along the crystallographic c-axis. These chains exhibit a staggered shift along the b-axis, as depicted in Fig. 1. Within the basal ab plane, the Co^{2+} spins form a weakly coupled, distorted triangular lattice. The combined effects of Hund's coupling and spin-orbit coupling (SOC) stabilize a $J_{\text{eff}} = 1/2$ state for the Co^{2+} ions[43]. Neutron diffraction reveals a ground-state magnetic structure below 1.97 K characterized by ferromagnetic ordering moments within each chain and antiferromagnetic ordering between chains. Experimentally, the easy magnetization axes of the Co^{2+} ions are tilted from the c axis by approximately $\pm 30^\circ$, with the sign of this tilt angle alternating between adjacent chains. To facilitate analysis using 2DCS, our work employs a simplified distorted Kitaev model considering only NN exchange interactions between cobalt ions. As shown in Fig. 1(b), we define a laboratory coordinate system $[x, y, z]$ by rotating the easy magnetization axis by $\gamma = 30^\circ$ around the b-axis, aligning the z-axis with the Ising easy direction. Due to the twist angle, we establish two local coordinate systems $[x', y', z']$ based on the distinct coupling directions \hat{n}_1 and \hat{n}_2 to project local interactions. These local frames are obtained by rotating the laboratory system by the twist angle θ around the x-axis respectively. We consider the anisotropic Heisenberg Hamiltonian in these local coordinates:

$$H_{\text{local}} = -J_{x'} \sum_i s_i^{x'} s_{i+1}^{x'} - J_{y'} \sum_i s_i^{y'} s_{i+1}^{y'} - J_{z'} \sum_i s_i^{z'} s_{i+1}^{z'}, \quad (1)$$

where $J_{x'}$, $J_{y'}$ and $J_{z'}$ are the NN magnetic exchange constants in the local frames. By transforming the model into the lab frame, we obtain the Hamiltonian for the TKM for NN exchange interactions as follows, see Appendix A:

$$\begin{aligned} H_{\text{TKM}} = & -J_{x'} \sum_i s_i^x s_{i+1}^x \\ & -J_{y'} \sum_i \left[\sin^2(\theta) s_i^z s_{i+1}^z + \cos^2(\theta) s_i^y s_{i+1}^y - \frac{\sin(2\theta)}{2} (-1)^i (s_i^z s_{i+1}^y + s_i^y s_{i+1}^z) \right] \\ & -J_{z'} \sum_i \left[\cos^2(\theta) s_i^z s_{i+1}^z + \sin^2(\theta) s_i^y s_{i+1}^y + \frac{\sin(2\theta)}{2} (-1)^i (s_i^y s_{i+1}^z + s_i^z s_{i+1}^y) \right] - h \sum_i s_i^y, \quad (2) \end{aligned}$$

here θ is the twist angle between the two NN \hat{n} directions, where \hat{n} is the bond-dependent Ising interaction direction as shown in Fig.1(c), h is the transverse magnetic field. At $\theta = 0^\circ$, the Ising nature of the Hamiltonian is dominant. The Kitaev nature becomes dominant at $\theta = 45^\circ$, which is not intuitive since the Kitaev interaction is the off-diagonal terms[41]. Comparison with the established exchange constant matrices yields the local coordinate exchange constants for CoNb_2O_6 :

$J_{x'} = 0.57$ meV, $J_{y'} = 0.51$ meV, and $J_{z'} = 2.64$ meV [40]. The unknown twist angle θ will be determined by fitting the experimental results of specific heat[34].

Next, we present the formalism of 2DCS for the twisted kitaev model. Based on the experimental procedure of 2DCS, we consider probing the Kitaev interaction in a spin system using two pulsed magnetic fields separated by a time interval τ_1 . The higher-order nonlinear response arising from the coherence induced by these pulses is measured after a further delay τ_2 following the second pulse. Setting the time of the first pulse at $t = 0$, the second pulse occurs at $t = \tau_1$. The α -component pulsed magnetic field signal can be written as [21, 26]:

$$B^\alpha(t) = B_0^\alpha \delta(t) + B_1^\alpha \delta(t - \tau_1), \quad (3)$$

The nonlinear magnetization response M_{NL}^α in the α -direction, measured at $t = \tau_1 + \tau_2$, is defined as the difference between the total magnetization induced by both pulses and the sum of the magnetizations induced by each pulse individually: $M_{NL}^\alpha(\tau_1 + \tau_2) = M_{B_0^\alpha B_1^\alpha}^\alpha(\tau_1 + \tau_2) - M_{B_0^\alpha}^\alpha(\tau_1 + \tau_2) - M_{B_1^\alpha}^\alpha(\tau_1 + \tau_2)$. Here, M_{NL}^α represents the nonlinear magnetization resulting from the coherent interaction of the two magnetic pulses, $M_{B_0^\alpha B_1^\alpha}^\alpha$ is the magnetization induced by both pulses, and $M_{B_0^\alpha}^\alpha$, $M_{B_1^\alpha}^\alpha$ are the responses to the individual pulses B_0^α and B_1^α , respectively. Expanding this expression in terms of linear and nonlinear susceptibilities yields [21, 26]:

$$\begin{aligned} M_{NL}^\alpha(\tau_2 + \tau_1)/2L = & \chi_{\alpha\alpha\alpha}^{(2)}(\tau_2, \tau_1) B_{\tau_1}^\alpha B_0^\alpha + \chi_{\alpha\alpha\alpha\alpha}^{(3)}(\tau_2, \tau_1, 0) B_{\tau_1}^\alpha B_0^\alpha B_0^\alpha \\ & + \chi_{\alpha\alpha\alpha\alpha}^{(3)}(\tau_2, 0, \tau_1) B_{\tau_1}^\alpha B_{\tau_1}^\alpha B_0^\alpha + O(B^4), \end{aligned} \quad (4)$$

where L is the number of sites. The n -th order susceptibility is given by [16, 26]:

$$\begin{aligned} \chi_{\alpha\cdots\alpha}^{(n)}(\tau_n, \cdots, \tau_1) = & \frac{i^n}{L} \Theta(\tau_1) \Theta(\tau_2) \cdots \Theta(\tau_n) \\ & \langle \left[\left[\cdots \left[\hat{M}^\alpha(\tau_n + \cdots + \tau_1), \hat{M}^\alpha(\tau_{n-1} + \cdots + \tau_1) \right], \cdots \right], \hat{M}^\alpha(0) \right] \rangle. \end{aligned} \quad (5)$$

Due to the slip symmetry of the system, the correlation function component in the second-order susceptibility vanishes under slip symmetry transformation [42]. Consequently, this work focuses primarily on the third-order susceptibility. Expanding the commutators in Eq. (5) yields the following expressions for the third-order susceptibility:

$$\chi_{\alpha\alpha\alpha\alpha}^{(3)}(\tau_2, \tau_1, 0) = -\frac{2}{L} \Theta(\tau_1) \Theta(\tau_2) \sum_{l=1}^4 \text{Im} \left[R_{\alpha\alpha\alpha\alpha}^{(l)}(\tau_2, \tau_1, 0) \right], \quad (6)$$

$$\chi_{\alpha\alpha\alpha\alpha}^{(3)}(\tau_2, 0, \tau_1) = -\frac{2}{L} \Theta(\tau_1) \Theta(\tau_2) \sum_{l=1}^4 \text{Im} \left[R_{\alpha\alpha\alpha\alpha}^{(l)}(\tau_2, 0, \tau_1) \right]. \quad (7)$$

The higher-order correlation functions $R_{\alpha\alpha\alpha\alpha}^{(l)}(t_3, t_2, t_1)$ in Eqs. (6) and (7) are defined as:

$$R_{\alpha\alpha\alpha\alpha}^{(1)}(t_3, t_2, t_1) = \langle \hat{M}^\alpha(t_3 + t_2 + t_1) \hat{M}^\alpha(t_2 + t_1) \hat{M}^\alpha(t_1) \hat{M}^\alpha(0) \rangle, \quad (8)$$

$$R_{\alpha\alpha\alpha\alpha}^{(2)}(t_3, t_2, t_1) = -\langle \hat{M}^\alpha(t_2 + t_1) \hat{M}^\alpha(t_3 + t_2 + t_1) \hat{M}^\alpha(t_1) \hat{M}^\alpha(0) \rangle. \quad (9)$$

$$R_{\alpha\alpha\alpha\alpha}^{(3)}(t_3, t_2, t_1) = -\langle \hat{M}^\alpha(t_1) \hat{M}^\alpha(t_3 + t_2 + t_1) \hat{M}^\alpha(t_2 + t_1) \hat{M}^\alpha(0) \rangle, \quad (10)$$

$$R_{\alpha\alpha\alpha\alpha}^{(4)}(t_3, t_2, t_1) = \langle \hat{M}^\alpha(t_1) \hat{M}^\alpha(t_2 + t_1) \hat{M}^\alpha(t_3 + t_2 + t_1) \hat{M}^\alpha(0) \rangle, \quad (11)$$

In this work, we compute the correlation functions $R_{\alpha\alpha\alpha\alpha}^{(l)}(t_3, t_2, t_1)$ using the Lanczos method as seen in Appendix B. The standard Lanczos method generates an M_L -dimensional Krylov subspace, within which we solve for M_L eigenstates. The correlation functions are then evaluated within this subspace. For example, $R_{\alpha\alpha\alpha\alpha}^{(1)}(\tau_2, 0, \tau_1)$ becomes:

$$R_{\alpha\alpha\alpha\alpha}^{(1)}(\tau_2, 0, \tau_1) = \frac{1}{Z} \sum_n e^{-\beta \epsilon_n} \sum_{p,q,v=0}^{M_L} \langle \Psi_n | \hat{M}^\alpha | \Psi_p \rangle \langle \Psi_p | \hat{M}^\alpha | \Psi_q \rangle \times \langle \Psi_q | \hat{M}^\alpha | \Psi_v \rangle \langle \Psi_v | \hat{M}^\alpha | \Psi_n \rangle e^{i(\epsilon_n - \epsilon_v)\tau_1} e^{i(\epsilon_n - \epsilon_p)\tau_2}, \quad (12)$$

where the states $|\Psi_n\rangle$ to $|\Psi_v\rangle$ are eigenvectors computed via the orthogonal Lanczos method and Z is the partition function. See Appendix B for the details of the simulation.

III. NUMERICAL RESULTS AND DISCUSSION

A. Determining the Twist Angle in TKM via Specific Heat Data

In the TKM, the twist angle governs the relative strength of the Kitaev couplings, which in turn profoundly affects both the ground state and excitation properties of the system. To achieve more reliable results, we further validate the values of the twist angle by incorporating constraints from thermodynamic experiments. The specific heat of the TKM as a function of temperature is plotted in Fig. 2. It is shown that the transition temperature is approximately 2.8 K and the specific heat vanishes below 1 K at a twist angle of $\theta = 20^\circ$, which is in consistent with experimental results [34]. As illustrated in the inset of Fig. 2(a), we computed the system-size dependence of the phase transition temperature, identified by the specific heat peak C/T , for various twist angles

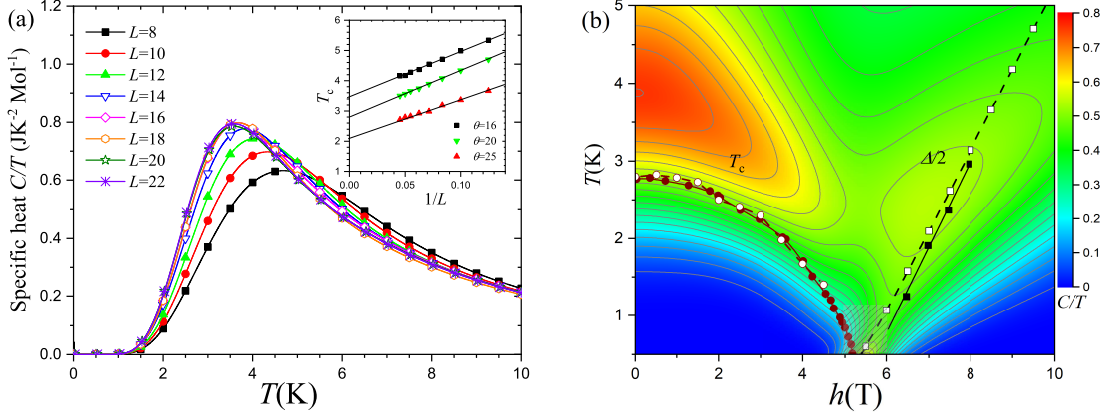


FIG. 2: (Color online) (a) The specific heat of the TKM for different chain length at $\theta=20^\circ$. Insite is the finite-size scaling result. (b) The phase diagrams of the twisted Kitaev model inferred from C/T with $\theta=20^\circ$ and chain length $L = 18$. The solid lines with circle and square symbols are the transition temperature T_c and gap Δ [34]. The dash lines with hollow circle and square symbols are the finite-size extrapolated numerical results for comparison.

to account for finite-size effects. With $\theta = 16^\circ$, the transition temperature increases to 3.4 K, significantly exceeding the experimental value. These findings support a twist angle of $\theta = 20^\circ$ for CoNb_2O_6 . Fig. 2(b) presents a phase diagram in the temperature–transverse magnetic field plane based on specific heat data. The critical field for the quantum phase transition from ferromagnetic to paramagnetic states is highly sensitive to the g -factor. Owing to strong spin–orbit coupling in CoNb_2O_6 , the g -factor is substantially larger than 2, with reported values for Co^{2+} ions typically ranging from 2.6 to 3.6 [35, 38–40, 44, 45]. To achieve better agreement with experiment, we employ a g -factor of 3.0 in Fig. 2(b). The solid line with circles denotes the experimental phase transition temperature T_c , while the line with squares indicates the experimental gap[34]. The finite-size extrapolated numerical results of the transition temperature and the excitation gap are also plotted for comparison. For $\theta = 20^\circ$, the boundary lines agree with experiment data very well. The TKM model accurately describes the transition from magnetically ordered to paramagnetic states, with a quantum critical point (QCP) at about $h_c = 5$ T[34]. The elementary excitations of TKM are spinons (kinks or domain wall) with the transverse magnetic field below the critical field h_c and the elementary excitations becomes magnon-like spin flips above h_c [36, 40, 46].

The dynamic spin structure factor defined as $S^{xx}(q, \omega) = \sum_v |\langle \Psi_v | S^x(q) | \Psi_0 \rangle|^2 \delta(\varepsilon_v - \varepsilon_0 - \omega)$ with twist angle $\theta = 20^\circ$ is shown in Fig. 3. In Fig. 3(a), a gapped continuum scattering arising

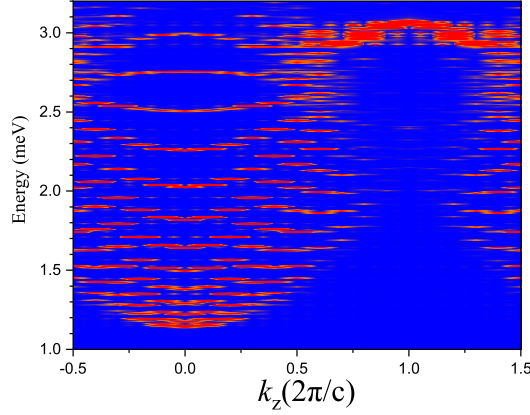


FIG. 3: (Color online) $S^{xx}(k, w)$ obtained by the exact diagonalization on a 20-site cluster with periodic boundary conditions at transverse fields $h = 0$

from spinon excitations appears near $k = 0$ in the energy range from 1.0 meV to 3.0V meV. The spectrum of the spinon excitations exhibit a quadratic dispersion shape due to off-diagonal interactions[36, 39, 44]. All these results establish that this model describes the spinon excitations in CoNb_2O_6 with only NN interactions. The above results demonstrate that the dispersions of spinons in this material, along with properties like specific heat and magnetic field-induced phase transitions, can be described by the TKM given in Eq. (2).

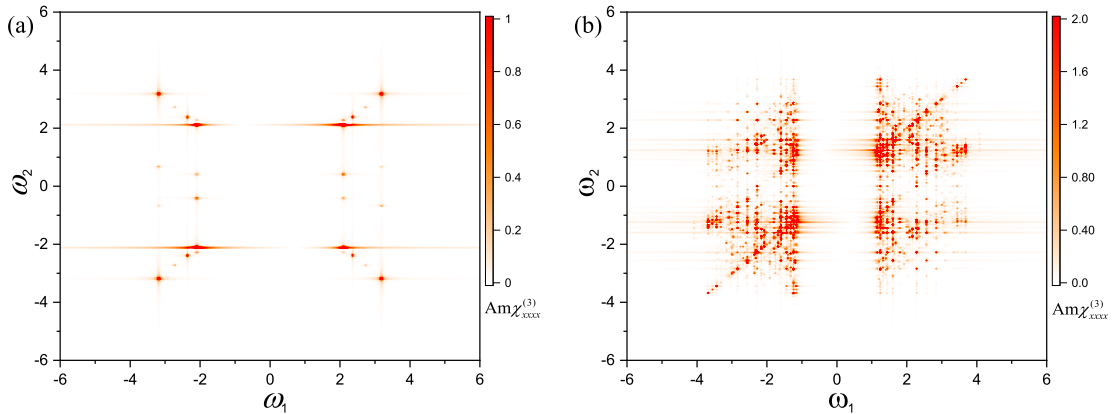


FIG. 4: (Color online) Two-dimensional amplitude spectrum of the third-order susceptibilities $\chi_{xxxx}^{(3)}(\omega_2, 0, \omega_1)$ for $\theta=0^\circ$ (a) and $\theta=20^\circ$ (b), respectively with chain length $L = 18$.

B. Two-dimensional coherent spectroscopy of finite twist angle

Our next goal is to detect the Kitaev components in CoNb_2O_6 through the 2DCS. The two-dimensional Fourier spectrums of the third-order susceptibilities $\chi_{xxxx}^{(3)}(\omega_2, 0, \omega_1)$ are plotted in Fig. 4. For comparision, we analyze the 2DCS at twist angle $\theta = 0^\circ$ firstly. At $\theta = 0^\circ$ the ground state of the Hamiltonian in Eq. (2) is ferromagnetic and the low-energy excitations are dominated by spinon. Thus, the spectral features near $\omega_1 = \omega_2 = \pm 2$ originate primarily from two-spinon single spin-flip excitation processes as shown in Figure 4(a)[25]. Within the Liouville space, the dominant contribution to these signal peaks arises from the paths that the quantum states $|\Psi_p\rangle$ and $|\Psi_v\rangle$ contain one spin flip, while the intermediate state $|\Psi_q\rangle$ contains either zero or two spin flips. The spectral signal near $\omega_2 = 0$ is contributed by bound two-spinon and two spin flips excitations. The corresponding Liouville space path is that each of the states $|\Psi_p\rangle$ and $|\Psi_v\rangle$ contains one spin flip, while the intermediate state $|\Psi_q\rangle$ contains two spin flips[25]. Unlike the 2D spectrum of Ising model, clustered discrete signals instead of a single one are observed near $(\omega_1, \omega_2) = (\pm 2, 0)$, which is induced by the finite value of J_x and J_y .

In contrast, the shape of the 2DCS changes sharply with $\theta = 20^\circ$ for realistic parameters in CoNb_2O_6 . As shown in Fig.4(b), the energy gap decreases to 1.06 meV. Furthermore, the finite twist angle leads to sharp non-rephasing signals along the diagonal in the first quadrant and it also gives rise to discrete spectral features in the fourth quadrants, which is different from the results given by Sim and Watanabe et al. [42, 46]. In their study, sharp rephasing signals were observed along the anti-diagonal in the fourth quadrant with only J_z exchange interaction ($J_x = J_y = 0$). The first reason is that the twist angle $\theta = 20^\circ$ of CoNb_2O_6 is significantly smaller. Secondly, the finite J_x and J_y exchange interactions in our model cause the rephasing signals to manifest as discrete structures, since the spinons become confinement bound states with finite J_x and J_y interactions [36, 46, 47]. Additionally, the characteristics of both the non-rephasing signal in the first quadrant and the discrete dot-like rephasing signals in the fourth quadrant show no significant variation with increasing system size, demonstrating that these signals are not finite-size effects, as seen Fig.11 in Appendix C.

To identify which processes contribute the rephase and non-rephase sigals in the susceptibilities, we study the Fourier transformation of R terms in Eq.(7) respectively. The terms of the third-order susceptibility in Eq.(7) can be described by four distinct double-sided Feynman diagrams (see Fig.10 in Appendix C) [16, 46]. To investigate the response processes of spinon excitations,

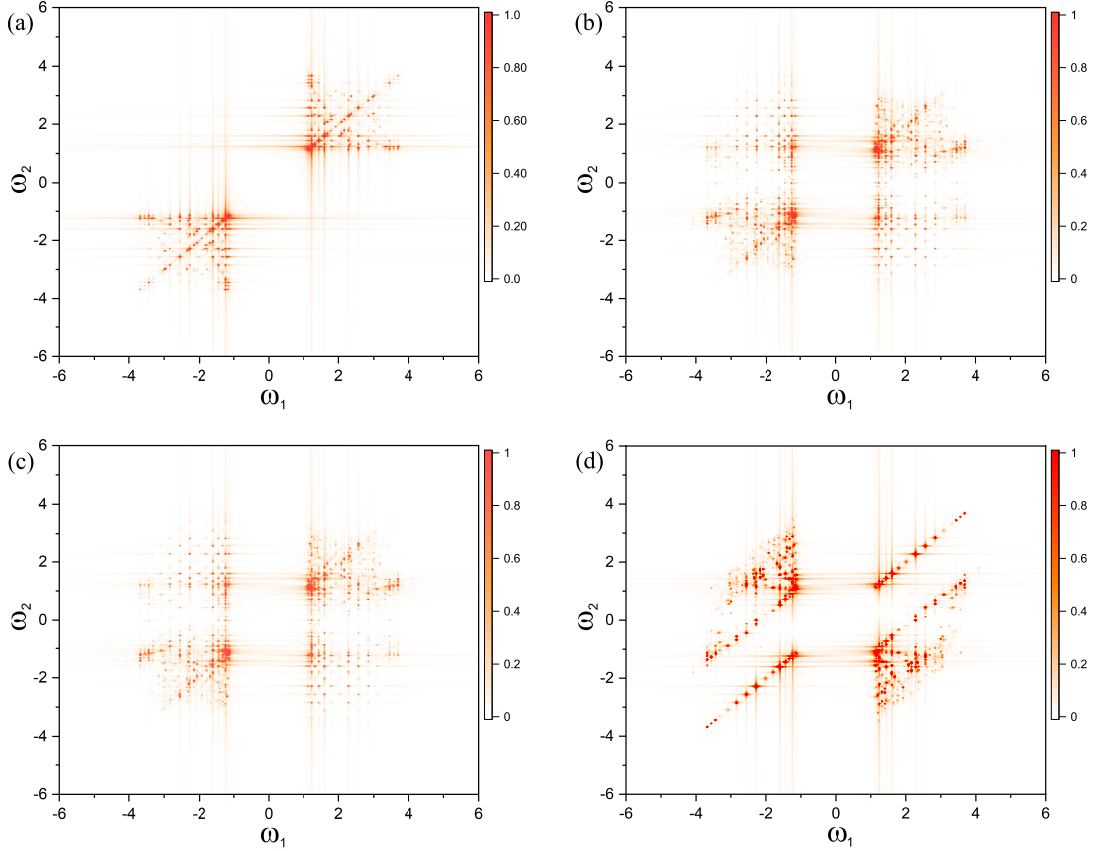


FIG. 5: (Color online) Two-dimensional amplitude spectrum of the four point correlation functions with $\theta=20^\circ$ and chain length $L = 18$, (a) $\text{Am}\mathcal{F}[\text{Im}R_{xxxx}^{(1)}(\tau_2, 0, \tau_1)]$ (b) $\text{Am}\mathcal{F}[\text{Im}R_{xxxx}^{(2)}(\tau_2, 0, \tau_1)]$ (c) $\text{Am}\mathcal{F}[\text{Im}R_{xxxx}^{(3)}(\tau_2, 0, \tau_1)]$ (d) $\text{Am}\mathcal{F}[\text{Im}R_{xxxx}^{(4)}(\tau_2, 0, \tau_1)]$. Here \mathcal{F} is the Fourier transformation.

the Fourier-transform spectras of the four-point correlation functions corresponding to these four diagrams are plotted in Fig. 5. As shown in Fig. 5(a) and (d), $R_{xxxx}^{(1)}(\tau_2, 0, \tau_1)$ and $R_{xxxx}^{(4)}(\tau_2, 0, \tau_1)$ contribute to non-rephasing signals. In Fig. 5(a), the dominant low-energy excitation processes for diagonal non-rephasing signals is that both the excited states $|\Psi_p\rangle$ and $|\Psi_v\rangle$ contain a pair of spinons, with the intermediate state $|\Psi_q\rangle$ being excited state ($|\Psi_q\rangle \neq |\Psi_n\rangle$). For $R_{xxxx}^{(4)}(\tau_2, 0, \tau_1)$ in Fig. 5(d), the diagonal non-rephasing signals in the first quadrant mainly attributed by the processes that the intermediate state $|\Psi_q\rangle$ is the ground state, while $|\Psi_p\rangle$ and $|\Psi_v\rangle$ are both two-kink single spin flip excited states. The noise signals distributed in the fourth quadrant of Fig. 5(d) come from the four-spinon excitation processes with $|\Psi_q\rangle \neq |\Psi_n\rangle$. The channel $R_{xxxx}^{(2)}(\tau_2, 0, \tau_1)$ and $R_{xxxx}^{(3)}(\tau_2, 0, \tau_1)$ contribute equally to the $\chi_{xxxx}^{(3)}(\omega_2, 0, \omega_1)$ as shown in Fig. 5(b) and (c) respectively. According to the double-sided Feynman diagrams as seen in Fig.10 in Appendix C, The

$R_{xxxx}^{(2)}(\tau_2, 0, \tau_1)$ and $R_{xxxx}^{(3)}(\tau_2, 0, \tau_1)$ are the primary contributors to the discrete rephase signals. The dominant excitation processes responsible for the rephasing signals involve a pathway with the state $|\Psi_q\rangle = |\Psi_n\rangle$.

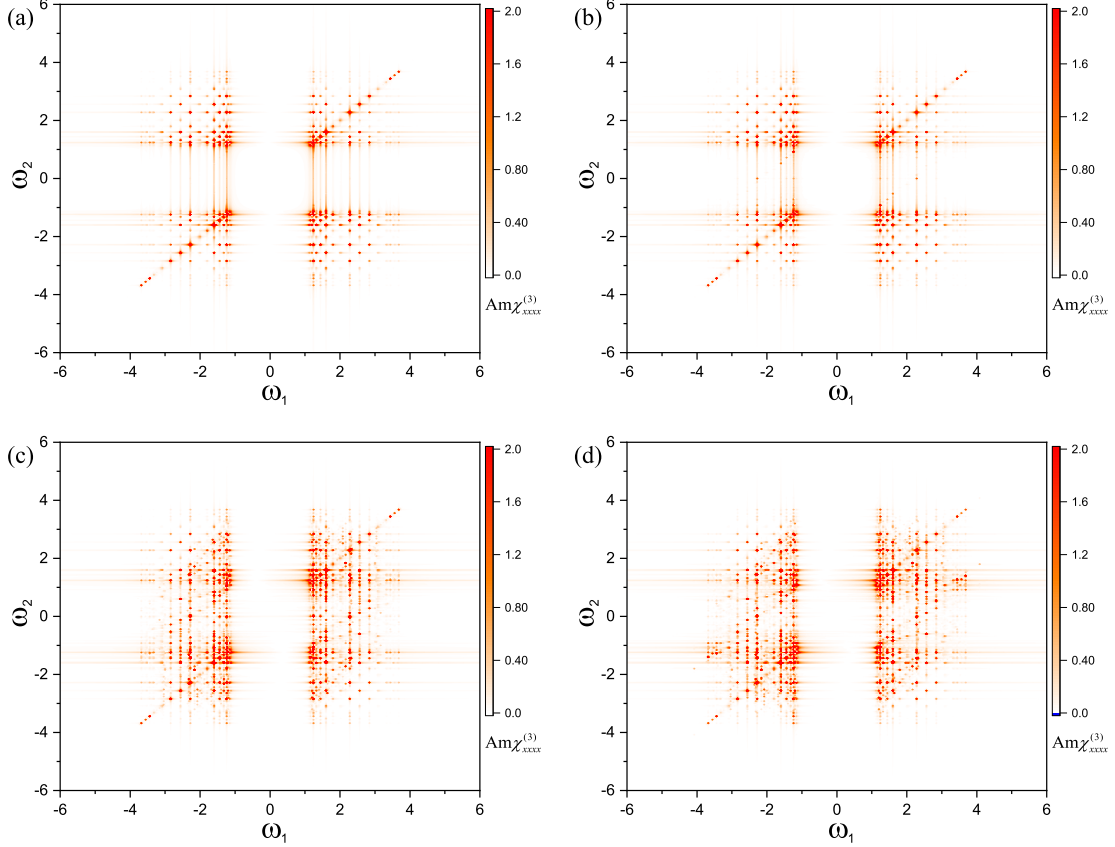


FIG. 6: (Color online) Two-dimensional amplitude spectrum of the third-order susceptibilities $\chi_{xxxx}^{(3)}(\omega_2, 0, \omega_1)$ for $\theta=20^\circ$ with two-kink single spin-flip (a), two-kink double spin-flip (b), four-kink single spin flip (c), and four-kink double spin-flip (d), projection approximation, respectively.

C. Resolved components in two-dimensional coherent spectroscopy

The projection approximation is an effective method for analyzing the contributions of various excitation processes to 2DCS[46, 48]. The low-energy excitations can be described by directly projecting the Hamiltonian onto the two-kink or four-kink subspace in the transverse-field Ising model under weak confinement conditions (e.g., $h_z \ll h_x$) [46]. However, it is not feasible to project the TKM Hamiltonian onto two-kink or four-kink Hilbert spaces because the ground-state

is not a simple fully-polarized ferromagnetic chain. To account for the contributions from various multi-kink excitations, we define the multi-kink state as

$$|n, l_{max}\rangle = \sum_{l_1, \dots, l_n} |j_1, l_1, \dots, j_n, l_n, \dots\rangle \quad (13)$$

where $l_{max} = \max\{l_1, l_2, \dots, l_n\}$, $l_i \leq l_{max}$, and

$$|j_1, l_1, \dots, j_n, l_n, \dots\rangle = |\dots \uparrow \uparrow \downarrow_{j_1} \dots \downarrow_{j_1+l_1-1} \uparrow \uparrow \dots \uparrow \uparrow \downarrow_{j_n} \dots \downarrow_{j_n+l_n-1} \uparrow \uparrow \dots\rangle. \quad (14)$$

we expand the total magnetic moment operator M^α of the system in terms of the number of kinks. The total magnetic moment is defined as

$$M^\alpha = \frac{1}{N_k} \sum_{k=1}^{N_k} \sum_{i=1}^N m_i^\alpha e^{i\vec{k} \cdot \vec{r}}. \quad (15)$$

The magnetic moment operator at each lattice site is projected onto the subspace of multi-kink multi-spin flips $m_{nl_{max}i}^\alpha = \mathcal{P}m_i^\alpha\mathcal{P}$, where \mathcal{P} is projection operator, which is defined as

$$\mathcal{P} = \sum_{n=1}^{N_{max}} \sum_{l_{max}=1}^{L_{max}} |n, l_{max}\rangle \langle n, l_{max}|. \quad (16)$$

By substituting this projected total magnetic moment operator into the higher-order susceptibility formula Eq.(5), the contributions of different spinon excitation processes to the 2DCS are obtained. As shown in Fig. 6(a) and Fig. 6 (b), the two-kink approximation already qualitatively reproduces the non-rephasing signals in the first quadrant and the discrete rephasing signals in the fourth quadrant. This indicates that the non-rephasing signal in the 2DCS of the TKM primarily originate from two-kink single spin-flip excitations. Nevertheless, the spectral weight within the region $-1 < \omega_2 < 1$ is reduced in Fig. 6(a) relative to that in Fig. 4(b). These missing signals are fully reproduced by the four-kink approximation, as shown in Fig. 6(c) and Fig. 6(d) , clearly revealing that these spectral weight is contributed by multi-spinon excitations.

To elucidate the quasiparticle excitations that play a dominant role in 2DCS, we project the excited state defined as $|\gamma\rangle = \sum_v \langle \Psi_v | M^\alpha | \Psi_v \rangle |\Psi_v\rangle$ to these multi-kink states as shown in Eq.(13). The projection distributions of the excited states are shown in Figure 7. The color represents the probability defined as $|\langle n, l_{max} | \gamma \rangle|^2$, where the number of spinons is given by $n_{\text{kink}} = 2n$. It is shown that two-kink single spin-flip and four-kink two to four spin-flips are the most prevalent excitations, which is similar to the results of transverse-field Ising model[36, 46].

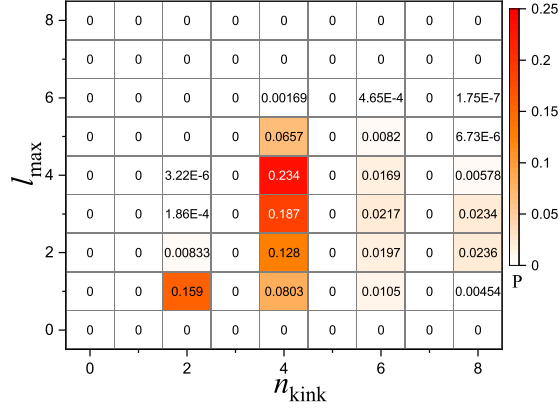


FIG. 7: (Color online) The projected probability $|\langle n, l_{\max} | \gamma \rangle|^2$ of multi-kink states in the excited wave function $|\gamma\rangle$ for $\theta=20^\circ$. Here, n_{kink} denotes the number of kinks and l_{\max} represents the maximum number of flipped spins between two kinks.

D. Tuning two-dimensional coherent spectroscopy with twist angle

To further investigate the effect of twist angle on 2DCS, the spectra at several typical angles are plotted in Fig. 8 for comparison. It is shown that the energy gap in the spectra significantly narrows as the twist angle increases, and it almost vanishes when the twist angle reaches 45° . This result aligns with the results obtained by Dagotto et al [41]. In their study, the energy gap decreases as the twist angle increases and the excitation gap of the system disappears at 45° . Furthermore, as the twist angle approaches 45° , the intensity of the z component of dynamic spin structure factor also increases markedly. Correspondingly, the signal intensity of $\chi_{zzz}^{(3),z}(\omega_2, 0, \omega_1)$ component also shows a clear enhancement when θ is near 45° in 2DCS spectra. The spectral signal near $\omega_2 = 0$ in 2DCS with $\theta = 0^\circ$ progressively weakens and evolves into a finite number of scattered points as the twist angle increases. The reason is that spinon excitations become confined as the twist angle increases, leading to weakened signals primarily contributed by two-kink two-spin-flip processes. Different from previous results, the rephasing signals in the fourth quadrant exhibit scattered features, originate from finite NN J_x and J_y interactions [42, 46]. Comparing the 2DCS in Fig. 4 and Fig. 8, it is revealed that diagonal signals are enhanced with increasing twist angle. This demonstrates the feasibility of using 2DCS to probe twist-angle variations in this system.

The squared total spin $\langle \mathbf{S} \cdot \mathbf{S} \rangle = \langle \sum_{i=1}^N s_i \sum_{j=1}^N s_j \rangle$ for the ground state and excited states is

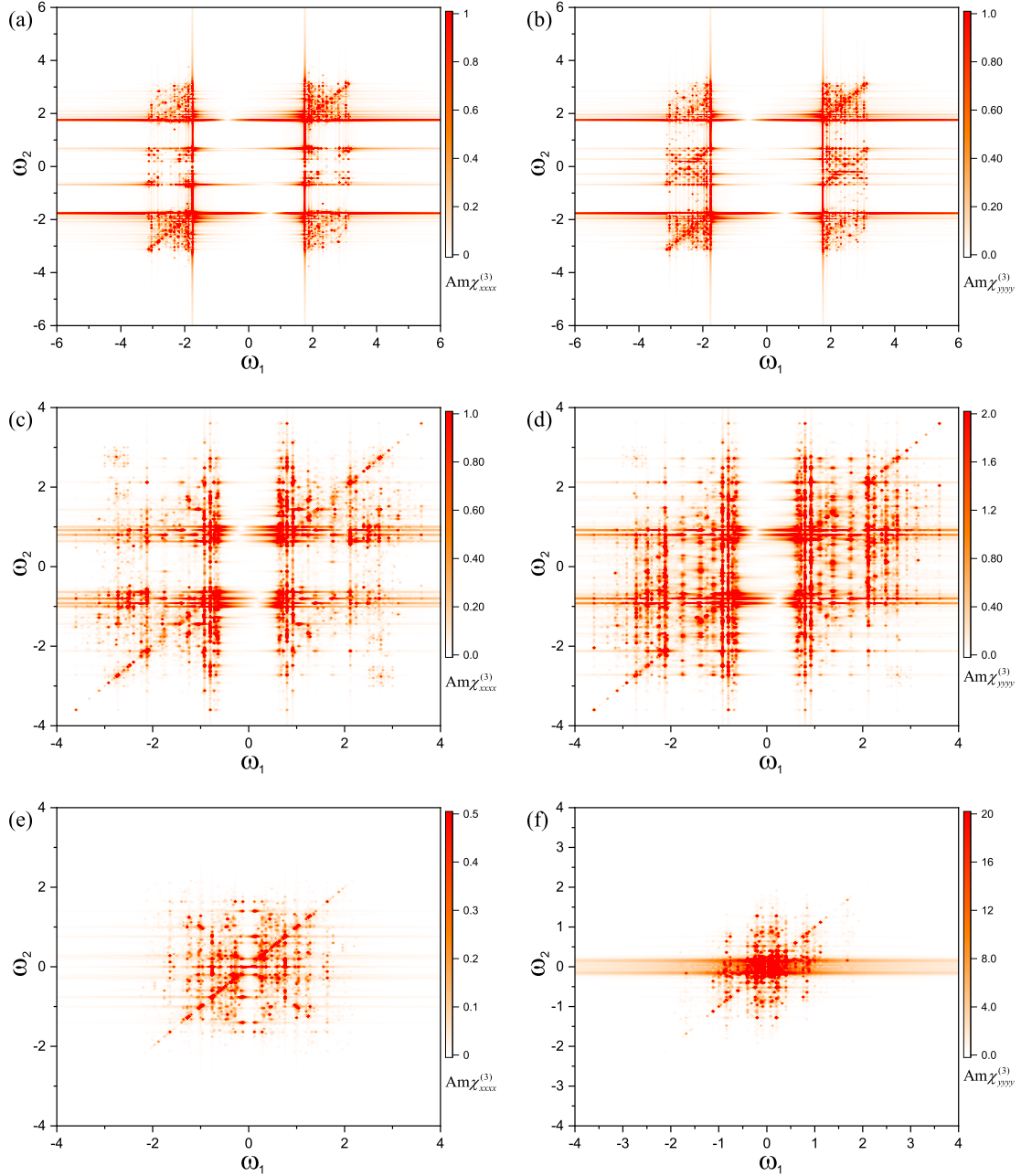


FIG. 8: (Color online) Two-dimensional amplitude spectrum of the third-order susceptibilities $\chi_{xxxx}^{(3)}(\omega_2, 0, \omega_1)$ and $\chi_{yyyy}^{(3)}(\omega_2, 0, \omega_1)$ with $\theta=10^\circ$ (a)(b), $\theta=30^\circ$ (c)(d), $\theta=45^\circ$ (e)(f), respectively. The chain length is $L = 18$.

plotted in Fig. 9 (a) and (b) respectively. As shown in Fig. 9(a), the squared total spin of the ground state remains nearly constant when the twist angle is below 30° . The squared total spin of the excited state in Fig. 9(b) indicates that approximately three to four spins are flipped, which is

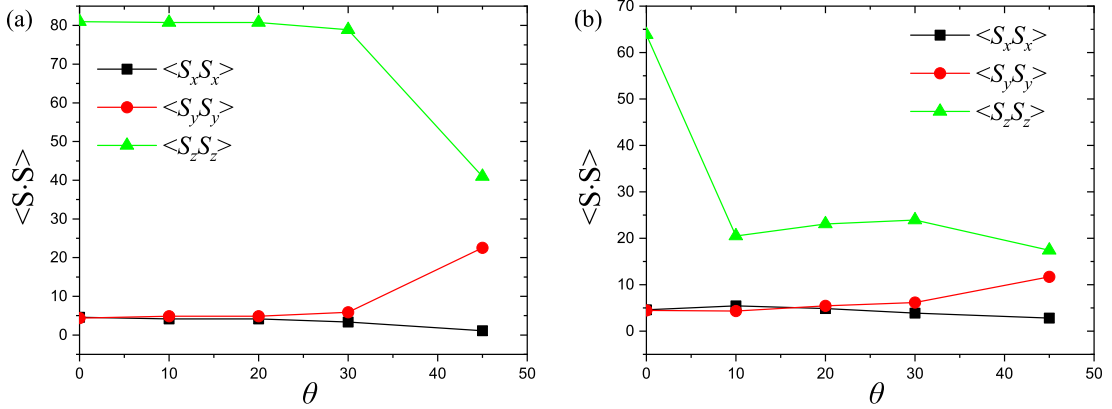


FIG. 9: (Color online) The squared total spin components of the ground state (a) and excited state $|\gamma\rangle$ (b) as a function of twist angle θ .

consistent with the results presented in Fig. 7. All the results of the total spin squared collectively demonstrate that the conclusions drawn for the specific twist angle $\theta = 20^\circ$ remain valid across the entire $10^\circ < \theta < 30^\circ$ regime.

IV. CONCLUSION

In summary, the TKM that incorporates NN exchange interactions is modified. The finite twisting angle leads to off-diagonal spin exchange interactions in the laboratory coordinate system. Then the 2DCS of the quasi-one-dimensional magnetic material CoNb_2O_6 is studied based on this model. The TKM exhibits sharp rephasing signals in the 2DCS with only the J_z exchange term[46], however, finite J_y couplings lead to the spin echo signals appearing discrete peaks in the fourth quadrant in our results. These results indicate that although the NN interactions along the x and y directions in the local coordinate system are significantly weaker than J_z , their influence on the rephasing signals in the 2DCS is also considerable. To investigate the contributions of different excitation processes to the 2DCS, we project the total magnetic moment operator onto the multi-spinon excited states. Our findings indicate that the diagonal non-rephasing signals and the discrete rephasing peaks in the fourth quadrant primarily originate from two-spinon excitations. Furthermore, by comparing the spectral signals at different twisting angles and conducting total spin analysis, we confirmed that the above physical picture remains valid for twisting angles $\theta < 30^\circ$.

It should be noted that the model employed in this study does not include the next-nearest-neighbor superexchange interactions and inter-chain spin couplings. Although the inclusion of these weak interactions would improve the results, one could be expected that it would not qualitatively alter the present results since these two spin coupling strengths are weaker than the NN spin couplings at least an order in magnitude. On the other hand, 2DCS has been widely applied to probe magnetic, superconducting, and spin-liquid systems due to its exceptional ability to resolve distinct quasiparticle excitations. Our work establishes the fact that even weak Kitaev interactions can generate characteristic spectral signatures, providing a pathway to detect subtle interactions in quantum materials.

Acknowledgments

X.-L. Yu is supported by the Guangdong Basic and Applied Basic Research Foundation (Grant No. 2023A1515011852) and this work is also supported by MOST 2022YFA1402701. The calculations were partly performed in Center for Computational Science of CASHIPS and Hefei Advanced Computing Center.

Appendix A: Detail of the twisted Kitaev model derivation

As shown in Fig. 1(b), we define a laboratory coordinate system $[x, y, z]$ by rotating the easy magnetization axis by $\gamma = 30$ around the b-axis, thus the y-axis aligned with the crystal basis vector b and the z-axis along the easy magnetization axis direction. Due to the presence of a twist angle, local coordinate systems $[x', y', z']$ are defined based on two distinct magnetic exchange directions. These local systems are obtained by rotating the laboratory coordinate system by the twist angle θ about the x-axis, yielding the transformations:

$$\begin{aligned}
 s_i^{x'} &= s_i^x \\
 s_i^{y'(\hat{n}_1)} &= -\sin(\theta)s_i^z + \cos(\theta)s_i^y \\
 s_i^{y'(\hat{n}_2)} &= \sin(\theta)s_i^z + \cos(\theta)s_i^y \\
 s_i^{z'(\hat{n}_1)} &= \cos(\theta)s_i^z + \sin(\theta)s_i^y \\
 s_i^{z'(\hat{n}_2)} &= \cos(\theta)s_i^z - \sin(\theta)s_i^y
 \end{aligned} \tag{A1}$$

Here θ is the twist angle between the two NN directions \hat{n} , where \hat{n} is the bond-dependent Ising interaction direction as shown in Fig.1(c). We consider the anisotropic Heisenberg Hamiltonian in these local coordinates:

$$H_{\text{local}} = -J_{x'} \sum_i s_i^{x'} s_{i+1}^{x'} - J_{y'} \sum_i s_i^{y'} s_{i+1}^{y'} - J_{z'} \sum_i s_i^{z'} s_{i+1}^{z'} \quad (\text{A2})$$

where $J_{x'}$, $J_{y'}$ and $J_{z'}$ are NN magnetic exchange constants in the local frames. Substituting the coordinate transformations into this Hamiltonian yields the TKM Hamiltonian for NN interactions:

$$\begin{aligned} H_{\text{TKM}} = & -J_{x'} \sum_i s_i^x s_{i+1}^x \\ & -J_{y'} \sum_i \left[\sin^2(\theta) s_i^z s_{i+1}^z + \cos^2(\theta) s_i^y s_{i+1}^y - \frac{\sin(2\theta)}{2} (-1)^i (s_i^z s_{i+1}^y + s_i^y s_{i+1}^z) \right] \\ & -J_{z'} \sum_i \left[\cos^2(\theta) s_i^z s_{i+1}^z + \sin^2(\theta) s_i^y s_{i+1}^y + \frac{\sin(2\theta)}{2} (-1)^i (s_i^y s_{i+1}^z + s_i^z s_{i+1}^y) \right], \end{aligned} \quad (\text{A3})$$

We write the NN magnetic interaction into matrix:

$$J = \begin{pmatrix} -J_{x'} & 0 & 0 \\ 0 & -J_{y'} \cos^2(\theta) - J_{z'} \sin^2(\theta) & (-1)^i (J_{y'} - J_{z'}) \frac{\sin(2\theta)}{2} \\ 0 & (-1)^i (J_{y'} - J_{z'}) \frac{\sin(2\theta)}{2} & -J_{y'} \sin^2(\theta) - J_{z'} \cos^2(\theta) \end{pmatrix} \quad (\text{A4})$$

Comparing to the results given by referens [40], We have

$$\begin{aligned} J_{x'} &= 0.57 \\ -J_{y'} \cos^2(\theta) - J_{z'} \sin^2(\theta) &= -0.67 \\ (J_{y'} - J_{z'}) \frac{\sin(2\theta)}{2} &= -0.56 \\ -J_{y'} \sin^2(\theta) - J_{z'} \cos^2(\theta) &= -2.48 \end{aligned} \quad (\text{A5})$$

Thus the values of exchange coupling constants are $J_{x'} = 0.57$ meV, $J_{y'} = 0.51$ meV, and $J_{z'} = 2.64$ meV.

Appendix B: Lanczos method

In the standard Lanczos method[50], the Krylov subspace $|\phi_0\rangle, H|\phi_0\rangle, \dots, H^{M-1}|\phi_0\rangle$ is constructed by iteratively computing matrix-vector products $|\phi\rangle = H|\phi_{n-1}\rangle$. Here, $|\phi_0\rangle$ is a random initial vector. Within this Krylov subspace, the Hamiltonian matrix can be reduced to a symmetric tridiagonal matrix of dimension $M_L \times M_L$ [51]. The eigenvalues and eigenvectors of the Hamiltonian can then be obtained by diagonalizing this tridiagonal matrix[50]. To preserve orthogonality among the basis vectors spanning the Krylov subspace, Gram-Schmidt orthogonalization is applied to all vectors during the computation. This approach is termed orthogonal Lanczos method. By diagonalizing the tridiagonal Hamiltonian within the Krylov subspace, one obtains the ground state and several excited-state eigenvalues and eigenvectors. These eigenstates are subsequently used in Eq. (12) to compute higher-order correlation functions and 2DCS.

Furthermore, the Lanczos method has been extended to low temperature and finite temperature situations[52, 53], which can be used to calculate the temperature-dependent magnetic and thermodynamic quantities of strongly correlated systems [54–58]. Based on high-temperature expansions[53], the finite-temperature Lanczos method (FTLM) expresses the thermodynamic average of an operator A and the exact partition function Z are given by the following equations:

$$\langle A \rangle = \frac{N_{st}}{ZR} \sum_{r=1}^R \sum_{j=0}^{M_L} e^{-\beta \varepsilon_j^r} \langle r | \Psi_j^r \rangle \langle \Psi_j^r | A | r \rangle \quad (B1)$$

$$\langle Z \rangle = \frac{N_{st}}{R} \sum_{r=1}^R \sum_{j=0}^{M_L} e^{-\beta \varepsilon_j^r} |\langle r | \Psi_j^r \rangle|^2, \quad (B2)$$

where $\beta = 1/k_B T$, k_B is the Boltzmann constant, and $|r\rangle$ denotes the initial random state $|\phi_0\rangle$. $|\Psi_j^r\rangle$ is the j -th eigenvector of the Hamiltonian calculated in the Krylov space with an initial vector $|\phi_0\rangle = |r\rangle$. Within the FTLM, a set of R distinct random initial vectors $|r\rangle$ is selected. ε_j^r is the eigenvalue corresponding to the eigenstate $|\Psi_j^r\rangle$, N_{st} and M_L denote the dimensions of the full Hamiltonian matrix and the Krylov subspace, respectively. To evaluate the thermodynamic statistical value $\langle A \rangle$, the eigenvalues ε_j^r and eigenvectors $|\Psi_j^r\rangle$ of the Hamiltonian are calculated via the Lanczos method using the initial random vector $|r\rangle$ firstly; subsequently, the thermodynamic average is obtained using Eqs. (B1) and (B2). In the present work, the finite-temperature Lanczos method is employed to calculate the specific heat of the TKM.

Appendix C: The n th order nonlinear susceptibility

In this Appendix, we provide detailed calculations for the nonlinear susceptibilities[16, 21, 26].

According to Eq.(5), the third order nonlinear susceptibility is given by (we choose the unit $\hbar = 1$)

$$\begin{aligned} \chi_{\alpha\alpha\alpha\alpha}^{(3)}(\tau_3, \tau_2, \tau_1) &= \frac{i^3}{L} \Theta(\tau_1) \Theta(\tau_2) \Theta(\tau_3) \\ &\times \langle [[M^\alpha(\tau_3 + \tau_2 + \tau_1), M^\alpha(\tau_2 + \tau_1)], M^\alpha(\tau_1)], M^\alpha(0) \rangle \end{aligned} \quad (\text{C1})$$

At two pulse limits of the three-pulse process, we get

$$\chi_{\alpha\alpha\alpha\alpha}^{(3)}(\tau_2, \tau_1, 0) = -\frac{i}{L} \Theta(\tau_1) \Theta(\tau_2) \sum_{l=1}^8 R_{\alpha\alpha\alpha\alpha}^{(l)}(\tau_2, \tau_1, 0), \quad (\text{C2})$$

$$\chi_{\alpha\alpha\alpha\alpha}^{(3)}(\tau_2, 0, \tau_1) = -\frac{i}{L} \Theta(\tau_1) \Theta(\tau_2) \sum_{l=1}^8 R_{\alpha\alpha\alpha\alpha}^{(l)}(\tau_2, 0, \tau_1). \quad (\text{C3})$$

In Eq.(C2) and Eq.(C3), the high-order correlation functions are

$$R_{\alpha\alpha\alpha\alpha}^{(1)}(t_3, t_2, t_1) = \langle \hat{M}^\alpha(t_3 + t_2 + t_1) \hat{M}^\alpha(t_2 + t_1) \hat{M}^\alpha(t_1) \hat{M}^\alpha(0) \rangle, \quad (\text{C4})$$

$$R_{\alpha\alpha\alpha\alpha}^{(2)}(t_3, t_2, t_1) = -\langle \hat{M}^\alpha(t_2 + t_1) \hat{M}^\alpha(t_3 + t_2 + t_1) \hat{M}^\alpha(t_1) \hat{M}^\alpha(0) \rangle, \quad (\text{C5})$$

$$R_{\alpha\alpha\alpha\alpha}^{(3)}(t_3, t_2, t_1) = -\langle \hat{M}^\alpha(t_1) \hat{M}^\alpha(t_3 + t_2 + t_1) \hat{M}^\alpha(t_2 + t_1) \hat{M}^\alpha(0) \rangle, \quad (\text{C6})$$

$$R_{\alpha\alpha\alpha\alpha}^{(4)}(t_3, t_2, t_1) = \langle \hat{M}^\alpha(t_1) \hat{M}^\alpha(t_2 + t_1) \hat{M}^\alpha(t_3 + t_2 + t_1) \hat{M}^\alpha(0) \rangle, \quad (\text{C7})$$

$$R_{\alpha\alpha\alpha\alpha}^{(5)}(t_3, t_2, t_1) = -\langle \hat{M}^\alpha(0) \hat{M}^\alpha(t_3 + t_2 + t_1) \hat{M}^\alpha(t_2 + t_1) \hat{M}^\alpha(t_1) \rangle, \quad (\text{C8})$$

$$R_{\alpha\alpha\alpha\alpha}^{(6)}(t_3, t_2, t_1) = \langle \hat{M}^\alpha(0) \hat{M}^\alpha(t_2 + t_1) \hat{M}^\alpha(t_3 + t_2 + t_1) \hat{M}^\alpha(t_1) \rangle, \quad (\text{C9})$$

$$R_{\alpha\alpha\alpha\alpha}^{(7)}(t_3, t_2, t_1) = \langle \hat{M}^\alpha(0) \hat{M}^\alpha(t_1) \hat{M}^\alpha(t_3 + t_2 + t_1) \hat{M}^\alpha(t_2 + t_1) \rangle, \quad (\text{C10})$$

$$R_{\alpha\alpha\alpha\alpha}^{(8)}(t_3, t_2, t_1) = -\langle \hat{M}^\alpha(0) \hat{M}^\alpha(t_1) \hat{M}^\alpha(t_2 + t_1) \hat{M}^\alpha(t_3 + t_2 + t_1) \rangle. \quad (\text{C11})$$

It is obvious that: $R_{\alpha\alpha\alpha\alpha}^{(5)} = -[R_{\alpha\alpha\alpha\alpha}^{(4)}]^*$, $R_{\alpha\alpha\alpha\alpha}^{(6)} = -[R_{\alpha\alpha\alpha\alpha}^{(3)}]^*$, $R_{\alpha\alpha\alpha\alpha}^{(7)} = -[R_{\alpha\alpha\alpha\alpha}^{(2)}]^*$, $R_{\alpha\alpha\alpha\alpha}^{(8)} = -[R_{\alpha\alpha\alpha\alpha}^{(1)}]^*$. We decompose the correlation function by inserting the resolution of identity in Krylov subspace. The third order nonlinear susceptibility is written as :

$$\begin{aligned} \chi_{\alpha\alpha\alpha\alpha}^{(3)}(\tau_3, \tau_2, \tau_1) = & \frac{i^3}{L} \Theta(\tau_1) \Theta(\tau_2) \Theta(\tau_3) \frac{1}{Z} \sum_n e^{-\beta \varepsilon_n} \sum_{pqv=0}^{M_{\text{krylov}}} [C_R + iC_I] \\ & \times \left\{ e^{\frac{i}{\hbar}(\varepsilon_n - \varepsilon_v)\tau_1} e^{\frac{i}{\hbar}(\varepsilon_n - \varepsilon_q)\tau_2} e^{\frac{i}{\hbar}(\varepsilon_n - \varepsilon_p)\tau_3} - e^{\frac{i}{\hbar}(\varepsilon_n - \varepsilon_v)\tau_1} e^{\frac{i}{\hbar}(\varepsilon_n - \varepsilon_q)\tau_2} e^{\frac{i}{\hbar}(\varepsilon_p - \varepsilon_q)\tau_3} \right. \\ & \left. - e^{\frac{i}{\hbar}(\varepsilon_n - \varepsilon_v)\tau_1} e^{\frac{i}{\hbar}(\varepsilon_p - \varepsilon_v)\tau_2} e^{\frac{i}{\hbar}(\varepsilon_p - \varepsilon_q)\tau_3} + e^{\frac{i}{\hbar}(\varepsilon_n - \varepsilon_v)\tau_1} e^{\frac{i}{\hbar}(\varepsilon_p - \varepsilon_v)\tau_2} e^{\frac{i}{\hbar}(\varepsilon_q - \varepsilon_v)\tau_3} \right\} \\ & + \frac{i^3}{L} \Theta(\tau_1) \Theta(\tau_2) \Theta(\tau_3) \frac{1}{Z} \sum_n e^{-\beta \varepsilon_n} \sum_{pqv=0}^{M_{\text{krylov}}} [C_R - iC_I] \\ & \times \left\{ -e^{\frac{i}{\hbar}(\varepsilon_v - \varepsilon_n)\tau_1} e^{\frac{i}{\hbar}(\varepsilon_v - \varepsilon_p)\tau_2} e^{\frac{i}{\hbar}(\varepsilon_v - \varepsilon_q)\tau_3} + e^{\frac{i}{\hbar}(\varepsilon_v - \varepsilon_n)\tau_1} e^{\frac{i}{\hbar}(\varepsilon_v - \varepsilon_p)\tau_2} e^{\frac{i}{\hbar}(\varepsilon_q - \varepsilon_p)\tau_3} \right. \\ & \left. + e^{\frac{i}{\hbar}(\varepsilon_v - \varepsilon_n)\tau_1} e^{\frac{i}{\hbar}(\varepsilon_q - \varepsilon_n)\tau_2} e^{\frac{i}{\hbar}(\varepsilon_q - \varepsilon_p)\tau_3} - e^{\frac{i}{\hbar}(\varepsilon_v - \varepsilon_n)\tau_1} e^{\frac{i}{\hbar}(\varepsilon_q - \varepsilon_n)\tau_2} e^{\frac{i}{\hbar}(\varepsilon_p - \varepsilon_n)\tau_3} \right\}, \end{aligned} \quad (\text{C12})$$

where $C_R + iC_I = \langle \Psi_n | M^\alpha | \Psi_p \rangle \langle \Psi_p | M^\alpha | \Psi_q \rangle \langle \Psi_q | M^\alpha | \Psi_v \rangle \langle \Psi_v | M^\alpha | \Psi_n \rangle$. By considering $\tau_2 = 0$ and $\tau_3 \rightarrow \tau_2$, we get the two pulse limit formula

$$\begin{aligned} \chi_{\alpha\alpha\alpha\alpha}^{(3)}(\tau_2, 0, \tau_1) = & \frac{i^3}{L} \Theta(\tau_1) \Theta(\tau_2) \frac{1}{Z} \sum_n e^{-\beta \varepsilon_n} \sum_{pqv=0}^{M_{\text{krylov}}} [C_R + iC_I] \\ & \times \left\{ e^{\frac{i}{\hbar}(\varepsilon_n - \varepsilon_v)\tau_1} e^{\frac{i}{\hbar}(\varepsilon_n - \varepsilon_p)\tau_2} - e^{\frac{i}{\hbar}(\varepsilon_n - \varepsilon_v)\tau_1} e^{\frac{i}{\hbar}(\varepsilon_p - \varepsilon_q)\tau_2} \right. \\ & \left. - e^{\frac{i}{\hbar}(\varepsilon_n - \varepsilon_v)\tau_1} e^{\frac{i}{\hbar}(\varepsilon_p - \varepsilon_q)\tau_2} + e^{\frac{i}{\hbar}(\varepsilon_n - \varepsilon_v)\tau_1} e^{\frac{i}{\hbar}(\varepsilon_q - \varepsilon_v)\tau_2} \right\} \\ & + \frac{i^3}{L} \Theta(\tau_1) \Theta(\tau_2) \frac{1}{Z} \sum_n e^{-\beta \varepsilon_n} \sum_{pqv=0}^{M_{\text{krylov}}} [C_R - iC_I] \\ & \times \left\{ -e^{\frac{i}{\hbar}(\varepsilon_v - \varepsilon_n)\tau_1} e^{\frac{i}{\hbar}(\varepsilon_v - \varepsilon_q)\tau_2} + e^{\frac{i}{\hbar}(\varepsilon_v - \varepsilon_n)\tau_1} e^{\frac{i}{\hbar}(\varepsilon_q - \varepsilon_p)\tau_2} \right. \\ & \left. + e^{\frac{i}{\hbar}(\varepsilon_v - \varepsilon_n)\tau_1} e^{\frac{i}{\hbar}(\varepsilon_q - \varepsilon_p)\tau_2} - e^{\frac{i}{\hbar}(\varepsilon_v - \varepsilon_n)\tau_1} e^{\frac{i}{\hbar}(\varepsilon_p - \varepsilon_n)\tau_2} \right\}. \end{aligned} \quad (\text{C13})$$

Applying a Fourier transform, the space-time Fourier transform of χ is expressed as follows

$$\begin{aligned} \chi_{\alpha\alpha\alpha\alpha}^{(3)}(\omega_2, 0, \omega_1) = & \frac{i}{ZL} \sum_n e^{-\beta \varepsilon_n} \sum_{pqv=0}^{M_{\text{krylov}}} [C_R + iC_I] F_{201}(\omega_1, \omega_2, \varepsilon_n, \varepsilon_p, \varepsilon_q, \varepsilon_v) \\ & + \frac{i}{ZL} \sum_n e^{-\beta \varepsilon_n} \sum_{pqv=0}^{M_{\text{krylov}}} [C_R - iC_I] F_{201}(\omega_1, \omega_2, -\varepsilon_n, -\varepsilon_p, -\varepsilon_q, -\varepsilon_v), \end{aligned} \quad (\text{C14})$$

where

$$\begin{aligned}
F_{201}(\omega_1, \omega_2, \varepsilon_n, \varepsilon_p, \varepsilon_q, \varepsilon_v) = & \\
& \left\{ \frac{1}{(\omega_1 + \varepsilon_n - \varepsilon_v + i0^+)(\omega_2 + \varepsilon_n - \varepsilon_p + i0^+)} \right. \\
& - \frac{1}{(\omega_1 + \varepsilon_n - \varepsilon_v + i0^+)(\omega_2 + \varepsilon_p - \varepsilon_q + i0^+)} \\
& - \frac{1}{(\omega_1 + \varepsilon_n - \varepsilon_v + i0^+)(\omega_2 + \varepsilon_p - \varepsilon_q + i0^+)} \\
& \left. + \frac{1}{(\omega_1 + \varepsilon_n - \varepsilon_v + i0^+)(\omega_2 + \varepsilon_q - \varepsilon_v + i0^+)} \right\}. \tag{C15}
\end{aligned}$$

For $\tau_1 = 0, \tau_3 \rightarrow \tau_2, \tau_2 \rightarrow \tau_1$ case, we obtain the formula as similiar as Eq.(C14):

$$\begin{aligned}
\chi_{\alpha\alpha\alpha\alpha}^{(3)}(\omega_2, \omega_1, 0) = & \frac{i}{ZL} \sum_n e^{-\beta\varepsilon_n} \sum_{pqv=0}^{M_{krylov}} [C_R + iC_I] F_{210}(\omega_1, \omega_2, \varepsilon_n, \varepsilon_p, \varepsilon_q, \varepsilon_v) \\
& + \frac{i}{ZL} \sum_n e^{-\beta\varepsilon_n} \sum_{pqv=0}^{M_{krylov}} [C_R - iC_I] F_{210}(\omega_1, \omega_2, -\varepsilon_n, -\varepsilon_p, -\varepsilon_q, -\varepsilon_v), \tag{C16}
\end{aligned}$$

where $F_{210}(\omega_1, \omega_2, \varepsilon_n, \varepsilon_p, \varepsilon_q, \varepsilon_v)$ is written as

$$\begin{aligned}
F_{210}(\omega_1, \omega_2, \varepsilon_n, \varepsilon_p, \varepsilon_q, \varepsilon_v) = & \\
& \left\{ \frac{1}{(\omega_1 + \varepsilon_n - \varepsilon_q + i0^+)(\omega_2 + \varepsilon_n - \varepsilon_p + i0^+)} \right. \\
& - \frac{1}{(\omega_1 + \varepsilon_n - \varepsilon_q + i0^+)(\omega_2 + \varepsilon_p - \varepsilon_q + i0^+)} \\
& - \frac{1}{(\omega_1 + \varepsilon_p - \varepsilon_v + i0^+)(\omega_2 + \varepsilon_p - \varepsilon_q + i0^+)} \\
& \left. + \frac{1}{(\omega_1 + \varepsilon_p - \varepsilon_v + i0^+)(\omega_2 + \varepsilon_q - \varepsilon_v + i0^+)} \right\}. \tag{C17}
\end{aligned}$$

In the calculation of the correlation function $C_R + iC_I$ based on the orthogonal Lanczos method, we utilize $M_L = 2048$ eigenstates. This ensures the maximum excitation energy considered sufficiently covers the spectral (energy) range of interest. The temperature parameter is set to $T = 1.0$ K. To reduce the number of channels in Liouville space, only correlation function terms with magnitudes exceeding 0.001 are included in the summation. Since the Fourier transform operates only over the positive time axis and the laser pulses are in the impulsive limit, the third-order susceptibility convolves with $[\delta(\omega_1 - \varepsilon_n - \varepsilon_v) + \mathcal{P}i/(\omega_1 - \varepsilon_n - \varepsilon_v)] [\delta(\omega_2 - \varepsilon_n - \varepsilon_p) + \mathcal{P}i/(\omega_2 - \varepsilon_n - \varepsilon_p)]$, where \mathcal{P} denotes the principal value integral. The principal value part introduces a weak $1/\omega$ broadening along both frequency axes. In our numerical implementation, the broadening width for the delta functions is set to 0.002, resulting in sharp features in the calculated 2DCS signal.

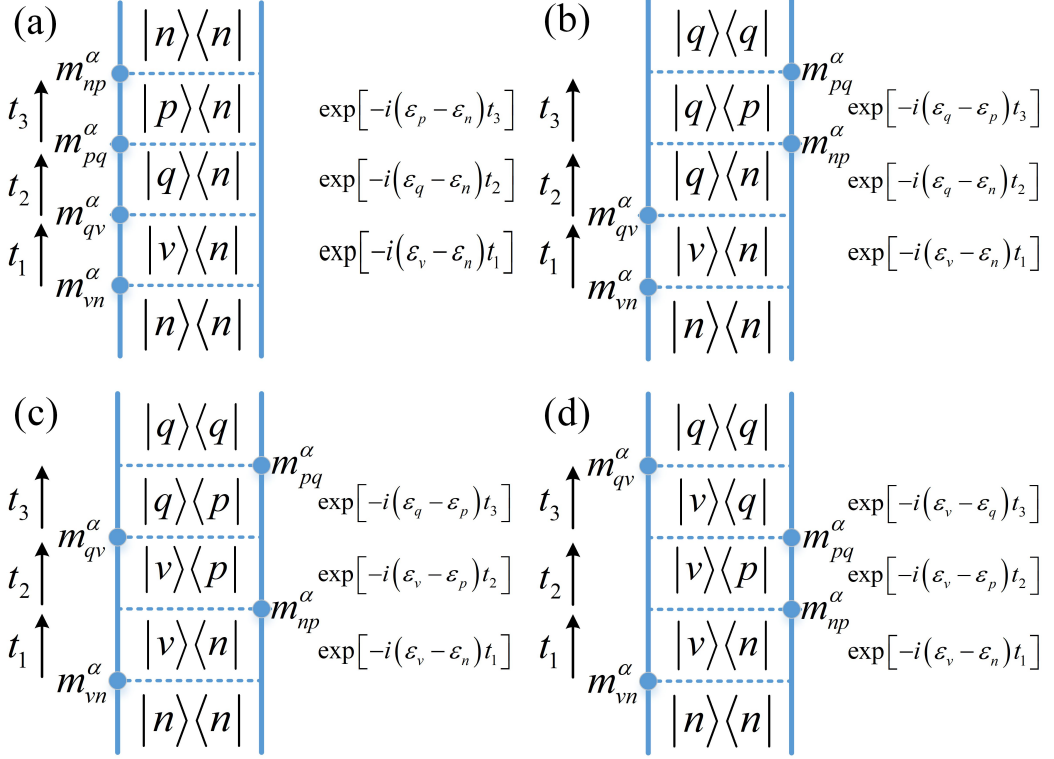


FIG. 10: (Color online) Double-sided Feynman diagrams for $R_{\alpha\alpha\alpha\alpha}^{(1)}$ (a), $R_{\alpha\alpha\alpha\alpha}^{(2)}$ (b), $R_{\alpha\alpha\alpha\alpha}^{(3)}$ (c) and $R_{\alpha\alpha\alpha\alpha}^{(4)}$ (d) processes that contributed to the third order coherent spectroscopy $\chi_{xxxx}^{(3)}(\omega_2, 0, \omega_1)$. Time evolves from bottom to top and dots represent bra or ket operations on the density matrix. Here $|n\rangle$ is the ground state $|\Psi_n\rangle$. $|v\rangle$ $|p\rangle$ and $|q\rangle$ denote excited states $|\Psi_v\rangle$ $|\Psi_p\rangle$ and $|\Psi_q\rangle$ of the Hamiltonian respectively .

Fig.10 displays Feynman diagrams for the four third-order excitation pathways $R_{\alpha\alpha\alpha\alpha}^{(1)}$ to $R_{\alpha\alpha\alpha\alpha}^{(4)}$ in two-dimensional coherent spectroscopy (2DCS). When $t_2 = 0$, $|\Psi_q\rangle = |\Psi_n\rangle$, $|\Psi_v\rangle = |\Psi_p\rangle$, the pathways represented in Figs. 10(b) and (c) contain the phase factor $\exp[-i(\epsilon_v - \epsilon_n)(t_1 - t_3)]$. This functional form indicates that these excitation processes generate the rephasing signal.

For comparation, we plotted the the two-dimensional amplitude spectrum of the third-order susceptibilities $\chi_{xxxx}^{(3)}(\omega_2, 0\omega_1)$ with chain length $L = 16$ and $L = 20$. The four-point correlation function $C_R + iC_I$ is calculated based on ORLM. The eigenvalues and eigenstates are obtained by diagonalizing the tridiagonal Hamiltonian matrix in Krylov space. As shown in Fig. 11 , the diagonal nonrephase signals are very sharpe.

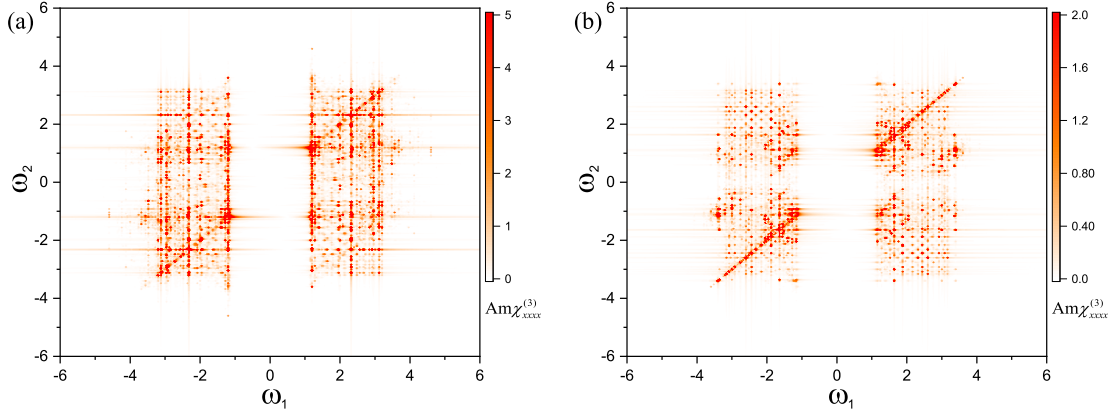


FIG. 11: (Color online) Two-dimensional amplitude spectrum of the third-order susceptibilities $\chi_{xxxx}^{(3)}(\omega_2, 0, \omega_1)$ with chain length $L=16$ (a) and $L=20$ (b).

- [2] L. Savary, and L. Balents, *Rep. Progr. Phys.* **80**, 016502 (2017).
- [3] L. Balents, *Nature* **464**, 199-208 (2010).
- [4] A. Kitaev, *Ann. Phys. (Amsterdam)* **321**, 2 (2006).
- [5] H. Takagi, T. Takayama, G. Jackeli, G. Khaliullin, and S. E. Nagler, *Nat. Rev. Phys.* **1**, 264-280 (2019).
- [6] J. S. Wen, S. L. Yu, S. Y. Li, W. Q. Yu, and J. X. Li, *npj Quantum Mater.* **4**, 12 (2019).
- [7] A. Banerjee, C. A. Bridges, J. Q. Yan, A. A. Aczel, L. Li, M. B. Stone, G. E. Granroth, M. D. Lumsden, Y. Yiu, J. Knolle, S. Bhattacharjee, D. L. Kovrizhin, R. Moessner, D. A. Tennant, D. G. Mandrus, and S. E. Nagler, *Nat. Mater.* **15**, 733-740 (2016).
- [8] A. Banerjee, J. Q. Yan, J. Knolle, C. A. Bridges, M. B. Stone, M. D. Lumsden, D. G. Mandrus, D. A. Tennant, R. Moessner, and S. E. Nagler, *Science* **356**, 1055-1059 (2017).
- [9] A. Banerjee, P. Lampen-Kelley, J. Knolle, C. Balz, A. A. Aczel, B. Winn, Y. Liu, D. Pajerowski, J. Q. Yan, C. A. Bridges, A. T. Savici, B. C. Chakoumakos, M. D. Lumsden, D. A. Tennant, R. Moessner, D. G. Mandrus, and S. E. Nagler, *npj Quantum Mater.* **3**, 8 (2018).
- [10] S. H. Do, S. Y. Park, J. Yoshitake, J. Nasu, Y. Motome, Y. S. Kwon, D. T. Adroja, D. J. Voneshen, K. Kim, T. H. Jang, J. H. Park, K. Y. Choi, and S. Ji, *Nat. Phys.* **13**, 1079-1084 (2017).
- [11] Y. Kasahara, K. Sugii, T. Ohnishi, M. Shimozawa, M. Yamashita, N. Kurita, H. Tanaka, J. Nasu, Y. Motome, T. Shibauchi, and Y. Matsuda, *Phys. Rev. Lett.* **120**, 217205 (2018).
- [12] O. Tanaka, Y. Mizukami, R. Harasawa, K. Hashimoto, K. Hwang, N. Kurita, H. Tanaka, S. Fujimoto, Y. Matsuda, E.-G. Moon, and T. Shibauchi, *Nat. Phys.* **18**, 429-435 (2022).
- [13] P. Czajka, T. Gao, M. Hirschberger, P. Lampen-Kelley, A. Banerjee, J. Q. Yan, D. G. Mandrus, S. E.

Nagler, and N. P. Ong, *Nat. Phys.* **17**, 915-919 (2021).

[14] T. Yokoi, S. Ma, Y. Kasahara, S. Kasahara, T. Shibauchi, N. Kurita, H. Tanaka, J. Nasu, Y. Motome, C. Hickey, S. Trebst, and Y. Matsuda, *Science* **373**, 568-572 (2021).

[15] C. Eichstaedt, Yi Zhang, P. Laurell, S. Okamoto, A. G. Eguiluz, and T. Berlijn, *Phys. Rev. B* **100**, 075110 (2019).

[16] S. Mukamel, *Principles of Nonlinear Optical Spectroscopy* (Oxford University Press, Rochester, New York, 1995).

[17] S. Mukamel, *Annu. Rev. Phys. Chem.* **51**, 691-729 (2000).

[18] D. M. Jonas, *Annu. Rev. Phys. Chem.* **54**, 425-463 (2003).

[19] N. T. Phuc, and P. Q. Trung, *Phys. Rev. B* **104**, 115105 (2021).

[20] Z. L. Li, M. Oshikawa, and Y. Wan, *Phys. Rev. X* **11**, 031035 (2021).

[21] Y. Wan, and N. P. Armitage, *Phys. Rev. Lett.* **122**, 257401 (2019).

[22] S. T. Cundiff, T. Zhang, A. D. Bristow, D. Karaiskaj, and X. Dai, *Acc. Chem. Res.* **42**, 1423-1432 (2009).

[23] J. Lu, X. Li, H. Y. Hwang, B. K. Ofori-Okai, T. Kurihara, T. Suemoto, and K. A. Nelson, *Phys. Rev. Lett.* **118**, 207204 (2017).

[24] Y. H. Qiang, V. L. Quito, T. V. Trevisan, and P. P. Orth, *Phys. Rev. Lett.* **133**, 126505 (2024).

[25] R. M. Nandkishore, W. Choi, and Y. B. Kim, *Phys. Rev. Res.* **3**, 013254 (2021).

[26] W. Choi, K. H. Lee, and Y. B. Kim, *Phys. Rev. Lett.* **124**, 117205 (2020).

[27] I. Cabrera, J. D. Thompson, R. Coldea, D. Prabhakaran, R. I. Bewley, T. Guidi, J. A. Rodriguez-Rivera, and C. Stock, *Phys. Rev. B* **90**, 014418 (2014).

[28] S. Kobayashi, S. Mitsuda, S. Hosaka, H. Tamatsukuri, T. Nakajima, H. Koorikawa, K. Prokeš, and K. Kiefer, *Phys. Rev. B* **94**, 134427 (2016).

[29] J. A. Ringler, A. I. Kolesnikov, and K. A. Ross, *Phys. Rev. B* **105**, 224421 (2022).

[30] C. M. Morris, R. V. Aguilar, A. Ghosh, S. M. Koohpayeh, J. Krizan, R. J. Cava, O. Tchernyshyov, T. M. McQueen, and N. P. Armitage, *Phys. Rev. Lett.* **112**, 137403 (2014).

[31] C. M. Morris, N. Desai, J. Viirok, D. Hüvonen, U. Nagel, T. Rööm, J. W. Krizan, R. J. Cava, T. M. McQueen, S. M. Koohpayeh, R. K. Kaul, and N. P. Armitage, *Nat. Phys.* **17**, 832-836 (2021).

[32] A. W. Kinross, M. Fu, T. J. Munsie, H. A. Dabkowska, G. M. Luke, S. Sachdev, and T. Imai, *Phys. Rev. X* **4**, 031008 (2014).

[33] S. Kobayashi, S. Hosaka, H. Tamatsukuri, T. Nakajima, S. Mitsuda, K. Prokeš, and K. Kiefer, *Phys.*

Rev. B **90**, 060412(R) (2014).

[34] T. Liang, S. M. Koohpayeh, J. W. Krizan, T. M. McQueen, R. J. Cava, and N. P. Qng, Nat.Commun **6**, 7611 (2015).

[35] S. Thota, S. Ghosh, R. Maruthi, D. C. Joshi, R. Medwal, R. S. Rawat, and M. S. Seehra, Phys. Rev. B **103**, 064415 (2021).

[36] R. Coldea, D. A. Tennant, E. M. Wheeler, E. Wawrzynska, D. Prabhakaran, M. Telling, K. Habicht, P. Smeibidl, and K. Kiefer, Science **327**, 177-180 (2010).

[37] S. Sachdev, Quantum Phase Transitions (Cambridge University Press, London, 1999), Chap.4.

[38] M. Fava, R. Coldea, and S. A. Parameswaran, Proc. Natl. Acad. Sci. USA **117**, 25219-25224 (2020).

[39] L. Woodland, I. Lovas, M. Telling, D. Prabhakaran, L. Balents, and R. Coldea, Phys. Rev. B **108**, 184417 (2023).

[40] C.A. Gallegos, and A.L. Chernyshev, Phys. Rev. B **109**, 014424 (2024).

[41] P. Laurell, G. Alvarez, and E. Dagotto, Phys. Rev. B **107**, 104414 (2023).

[42] G. Sim, F. Pollmann, and J. Knolle, Phys. Rev. B **108**, 134423 (2023).

[43] C. Heid, H. Weitzel, P. Burlet, M. Bonnet, W. Gonschorek, T. Vogt, J. Norwig, and H. Fuess, J. Magn. Magn. Mater **151**, 123 (1995).

[44] L. Woodland, D. Macdougal, I. M. Cabrera, J. D. Thompson, D. Prabhakaran, R. I. Bewley, and R. Coldea, Phys. Rev. B **108**, 184416 (2023).

[45] D. C. Churchill, and H. Y. Kee, Phys. Rev. Lett. **133**, 056703 (2024).

[46] Y. Watanabe, S. Trebst, and C. Hickey, Phys. Rev. B **110**, 134443 (2024).

[47] S.B. Rutkevich, J. Stat. Mech.: Theory Exp. **2010**, P07015 (2010).

[48] G. Sim, J. Knolle, and F. Pollmann, Phys. Rev. B **107**, L100404 (2023).

[49] W. Yang, C. Xu, S. Ma, A. Nocera, and I. Affleck, Phys. Rev. B **112**, 035104 (2025).

[50] J. Cullum and R. A. Willoughby, Lanczos Algorithms for Large Symmetric Eigenvalue Computations: Programs in Progress in Scientific Computing. Vol. 3, Ed. Birkhauser, (Boston, 1985).

[51] A. Avella and F. Mancini, Strongly Correlated Systems: Numerical Methods Springer (Heidelberg, 2013).

[52] M. Aichhorn, M. Daghofer, H. G. Evertz, and W. V. D. Linden, Phys. Rev. B **67**, 161103(R) (2003).

[53] J. Jaklic, and P. Prelovsek, Phys. Rev. B **49**, 5065(R) (1994).

[54] I. Zerec, B. Schmidt, and P. Thalmeier, Phys. Rev. B **73**, 245108 (2006).

[55] P. Horsch, J. Jaklič, and F. Mack, Phys. Rev. B **59**, 6217 (1999).

- [56] K. Haule, J. Bonča, and P. Prelovšek, Phys. Rev. B **61**, 2482 (2000).
- [57] C. S. Hellberg, J. Appl. Phys. **89**, 6627-6629 (2001).
- [58] S. Q. Jia, Y. M. Quan, L. J. Zou, and H. Q. Lin, Ann.Phys.(Berlin) **534**, 2200012 (2022).
- [59] J. C. Slater, Phys. Rev. **35**, 509 (1930).